Gamma-Ray Eclipses and Orbital Modulation Transitions in the Candidate Redback 4FGL J1702.7–5655

R.H.D. Corbet, L. Chomiuk, J.B. Coley, G. Dubus, P.G. Edwards, N. Islam, V.A. Mcbride, J. Stevens, J. Strader, S.J. Swihart, et al.

The Astrophysical Journal, 935:2 (15pp), 2022 August 10 https://doi.org/10.3847/1538-4357/ac6fe2

Gamma-Ray Eclipses and Orbital Modulation Transitions in the Candidate Redback 4FGL J1702.7–5655

R. H. D. Corbet[1,2], L. Chomiuk[3], J. B. Coley[4,5], G. Dubus[6], P. G. Edwards[7], N. Islam[1], V. A. McBride[8], J. Stevens[7], J. Strader[3], S. J. Swihart[9], and L. J. Townsend[10]

[1] University of Maryland, Baltimore County, and X-ray Astrophysics Laboratory, Code 662 NASA Goddard Space Flight Center, Greenbelt Rd., MD 20771, USA
[2] Maryland Institute College of Art, 1300 W Mt Royal Ave, Baltimore, MD 21217, USA
[3] Department of Physics and Astronomy, Michigan State University, East Lansing, MI 48824, USA
[4] Department of Physics and Astronomy, Howard University, Washington, DC 20059, USA
[5] CRESST/Code 661 Astroparticle Physics Laboratory, NASA Goddard Space Flight Center, Greenbelt Rd., MD 20771, USA
[6] Institut de Planétologie et d'Astrophysique de Grenoble, Univ. Grenoble Alpes, CNRS, F-38000 Grenoble, France
[7] Commonwealth Scientific and Industrial Research Organisation Astronomy and Space Science, PO Box 76, Epping, New South Wales 1710, Australia
[8] Department of Astronomy, University of Cape Town, Private Bag X3, Rondebosch, 7701, South Africa
[9] National Research Council Research Associate, National Academy of Sciences, Washington, DC 20001, USA, resident at Naval Research Laboratory, Washington, DC 20375, USA
[10] South African Astronomical Observatory, PO Box 9, Observatory, 7935, South Africa
Received 2021 December 19; revised 2022 April 19; accepted 2022 May 13; published 2022 August 8

Abstract

Observations with the Fermi Large Area Telescope (LAT) of the gamma-ray source 4FGL J1702.7−5655, previously classified as a candidate millisecond pulsar, show highly significant modulation at a period of 0.2438033 days (∼5.85 hr). Further examination of the folded light curve indicates the presence of narrow eclipses, suggesting that this is a redback binary system. An examination of the long-term properties of the modulation over 13 years of LAT observations indicates that the orbital modulation of the gamma rays changed from a simple eclipse before early 2013 to a broader, more easily detected quasi-sinusoidal modulation. In addition, the time of the eclipse shifts to ∼0.05 later in phase. This change in the orbital modulation properties, however, is not accompanied by a significant overall change in gamma-ray flux or spectrum. The quasi-sinusoidal component peaks ∼0.5 out of phase with the eclipse, which would indicate inferior conjunction of the compact object in the system. Swift X-ray Telescope observations reveal a possible X-ray counterpart within the LAT error ellipse. However, radio observations obtained with the Australia Telescope Compact Array do not detect a source in the region. 4FGL J1702.7−5655 appears to have changed its state in 2013, perhaps related to changes in the intrabinary shock in the system. We compare the properties of 4FGL J1702.7−5655 to those of other binary millisecond pulsars that have exhibited orbital modulation in gamma-rays.

Unified Astronomy Thesaurus concepts: Gamma-ray sources (633); Low-mass x-ray binary stars (939); Millisecond pulsars (1062); Neutron stars (1108); Eclipsing binary stars (444)

1. Introduction

1.1. Binary Millisecond Pulsars

Millisecond pulsars (MSPs) are pulsars with short pulse periods, but which are apparently old, as indicated by their slow spin-down rates. They are believed to be descended from low-mass X-ray binaries (LMXBs). Some MSPs are found in so-called spider binaries with a low-mass companion that is being ablated by the wind from the pulsar (e.g., Roberts 2013). Spider binaries are generally divided into black widow systems, in which the companion has a very low mass and may be degenerate, and redbacks, in which the companion is a near main-sequence star. An intrabinary shock (IBS) is thought to exist between the winds from the pulsar and its companion, and this can be the site of X-ray and radio emission (e.g., Gentile et al. 2014; Roberts et al. 2014; Kandel et al. 2019; van der Merwe et al. 2020). Orbitally modulated emission is commonly seen in X-rays, associated with accelerated particles in the IBS, and at radio wavelengths, where eclipses can be caused by scattering in dense ionized material. The optical emission is dominated by the light from the pulsar's companion, and this is generally modulated on the orbital period due to both gravitational ellipsoidal distortion and heating of the side of the companion that faces the pulsar (e.g., Breton et al. 2013).

Several redbacks have been seen to change between states in which the primary power source is the rotational energy of the neutron star and states in which accretion is occurring from the companion, and it becomes an LMXB. These are called transitional millisecond pulsars (tMSPs: e.g., Papitto & de Martino 2022). In tMSPs, three states are generally identified: (i) a pulsar state in which the pulsar is the power source in the system and no accretion occurs; (ii) accretion states in which accretion onto the surface of the neutron star occurs; (iii) a subluminous disk state in which rapid changes on timescales as short as ∼10 s can occur between high and low X-ray flux levels, including intermittent flares. Gamma-ray brightening may accompany a change from the rotation-powered state to the subluminous state.

The Large Area Telescope (LAT) on board the Fermi Gamma-ray Space Telescope has been surveying the gamma-ray sky above 100 MeV since 2008, and it has now identified more than 5000 sources. Of these, a significant number (>260; e.g., Grießmeier et al. 2021) have been identified as pulsars, a large fraction of which are MSPs.[11] Detection of periodic orbital modulation in

[11] https://confluence.slac.stanford.edu/display/GLAMCOG/Public+List+of+LAT-Detected+Gamma-Ray+Pulsars

MSPs at gamma-ray energies is relatively uncommon compared to modulation at other energies. 4FGL J0427.8−6704 (3FGL J0427.9−6704) was previously found to exhibit eclipses in gamma-rays, X-rays, and in the optical (Strader et al. 2016; Kennedy et al. 2020) at a period of ∼0.366 days. More recently, Clark et al. (2021b) found what they described as "subtle" gamma-ray eclipses in four systems: 4FGL J1048.6+2340 (PSR J1048+2339), 4FGL J1816.5+4510 (PSR J1816+4510), 4FGL J2129.8−0428 (PSR J2129-0429), and PSR B1957+20. The detection of these eclipses exploited orbital ephemerides obtained from radio and gamma-ray pulse timing, which give both the orbital period and the epoch of expected eclipse.

We have been conducting a search for previously unrecognized gamma-ray emitting binaries in the Fermi-LAT catalogs by searching for periodic modulation of the LAT flux. This has enabled us to detect several high-mass systems (Corbet et al. 2019, and references therein). Here we present the detection of strong periodic gamma-ray modulation in LAT observations of the candidate redback system 4FGL J1702.7−5655. We find that it exhibits periodic dips in its light curve that are consistent with eclipses in a redback system. In addition, an investigation of the multiyear behavior indicates a change in modulation properties from just a periodic dip to quasi-sinusoidal modulation together with a dip at a slightly later phase. We also searched for X-ray and radio counterparts of 4FGL J1702.7−5655 using the Swift X-ray Telescope (XRT) and the Australia Telescope Compact Array (ATCA), respectively, and identify a possible X-ray counterpart although no counterpart is detected at radio wavelengths. We compare the gamma-ray modulation in 4FGL J1702.7−5655 to that in other systems, and speculate on the cause of the change in orbital modulation. Unless otherwise noted, uncertainties are given at the 1σ level.

1.2. Previous Observations of 4FGL J1702.7−5655

4FGL J1702.7−5655 is in the fourth LAT catalog (Abdollahi et al. 2020), and counterparts were also present in the third catalog (3FGL J1702.8−5656; Acero et al. 2015), the LAT eight-year source list[12] (FL8Y J1702.7-5654), the second catalog (2FGL J1702.5-5654; Nolan et al. 2012), and the first catalog (1FGL J1702.4-5653; Abdo et al. 2010). It may also be associated with the AGILE gamma-ray source 2AGL J1703−5705 (Bulgarelli et al. 2019). Saz Parkinson et al. (2016) undertook a classification of sources in the 3FGL catalog into pulsars and active galactic nuclei—the two main categories of identified LAT sources. From this analysis, they found that 3FGL J1702.8−5656 was most likely to be a millisecond pulsar. 3FGL J1702.8−5656 was included in a search for gamma-ray pulsations from Fermi LAT observations for frequencies <1520 Hz by Clark et al. (2017) and Wu et al. (2018), but none were reported. In addition, 3FGL J1702.8−5656 was included in a search for radio pulsations using the Parkes telescope by Camilo et al. (2015) made with 125 μs time resolution, and none were found from this source.

2. Observations and Analysis

2.1. Gamma-ray Observations and Analysis

The Fermi LAT (Atwood et al. 2009; Ajello et al. 2021) is a pair-conversion telescope sensitive to gamma-ray photons with energies between ∼20 MeV and >300 GeV. The LAT data used in this paper were obtained between 2008 August 4 and 2021 August 19 (MJD 54,682 to 59,445). During this time, Fermi was primarily operated in sky-survey mode. Until 2018, the LAT pointing position was alternately rocked away from the zenith to the orbit north for one spacecraft orbit, then toward the orbit south for one orbit. In this way, the entire sky was observed every two spacecraft orbits, approximately every three hours. After a failure of the drive for one solar array, changes were made to the sky-survey profiles, but coverage of the entire sky was maintained in the long term (Ajello et al. 2021).

Our search for new gamma-ray binaries followed similar procedures to those described in Corbet et al. (2019). For the LAT analysis, we used the `fermitools` version `1.0.1` with the updated Pass 8 LAT data files (P8R3; Bruel et al. 2018) and the weekly photon files provided by the Fermi Science Support Center, which include precomputed diffuse response columns. Light curves covering an energy range of 100 MeV to 500 GeV were created for all 4FGL DR2 sources using time bins of 500 s. Times when sources were closer than 5° to the Sun were excluded, but no filtering was applied for the distance from the Moon. The light curves were obtained using a variant of aperture photometry, where we estimate the probability p that each photon comes from a source of interest and sum these probabilities (e.g., Kerr 2011; Fermi LAT Collaboration et al. 2012; Kerr 2019). To facilitate this, model files were created for each source using `make4FGLxml` including sources from the 4FGL DR2 catalog within a 10-degree radius from the source. Photon probabilities were calculated using `gtsrcprob` and then summed for a 3-degree radius aperture centered on each source. We used `gtbin` to create the initial light curves, but then replaced the integer `COUNTS` column with a floating-point `RCOUNTS` column containing the calculated summed probabilities. The exposure for each time bin was calculated using `gtexposure` to obtain the probability-weighted rate in units of p ph cm^{-2} s^{-1}, and times were corrected to the solar system barycenter with `gtexposure`. We note that although the use of probability photometry generally increases the signal-to-noise ratio of the light curves, it affects the photometric properties as probabilities are based on a constant source brightness. Thus, when a source is brighter than the model predicts, the probability of a photon coming from the source is underestimated, and when the source is fainter than the model prediction, the probability is overestimated (e.g., Kerr 2019). This results in a reduction of the apparent amplitude of any variability.

Power spectra of these LAT light curves were calculated using discrete Fourier transforms (DFT), weighting each data point's contribution by its relative exposure after first subtracting the mean count rate. This is beneficial because the substantial exposure changes from one time bin to the next. We note that while the time bins produced by `gtbin` are evenly spaced, but have gaps, this is no longer the case after the barycenter correction. However, even spacing is not required for calculation of a DFT. The use of weighting, however, does not change the intrinsic statistical properties of the power spectrum (Zechmeister & Kürster 2009; VanderPlas 2018), and the powers are expected to be distributed given by an exponential probability function. We normalize the computed powers to have an average power of unity. The power spectra cover a period range from 0.05 days (1.2 hr) to the length of the light curve, i.e., ∼4762 days, giving ∼95,246 independent frequencies. This is the same period range as we previously used in our searches (Corbet et al. 2016, 2019). While this range was primarily chosen to facilitate

[12] https://fermi.gsfc.nasa.gov/ssc/data/access/lat/fl8y/

a search for high-mass binaries, encompassing the relatively short 0.2-day period of Cygnus X-3 (4FGL J2032.6+4053) for which modulation of the LAT flux is already known (e.g., Corbel et al. 2012), we can potentially detect periodic modulation from any type of source in this range. The power spectra were oversampled by a factor of 5 compared to the nominal resolution, which we take to be the inverse of the length of the light curve (T; e.g., VanderPlas 2018, and references therein), i.e., $\sim 1/4762$ days^{-1}. As has been noted by several authors, if the power spectrum is not oversampled, then the measured power of a signal will be lower than the true power by a factor that ranges between $\sim$0.405 and 1, with a mean of $\sim$0.773 (e.g., van der Klis 1989; Vaughan 2005; VanderPlas 2018). The lowest measured power will occur if the signal frequency lies halfway between the sampling intervals. We also note that the same effect will also apply to noise peaks in the power spectrum. For the strongest peak in each power spectrum, the false-alarm probability (FAP; Scargle 1982), the estimated probability of a signal reaching a power level by chance assuming white noise, was calculated,

$$FAP = 1 - [1 - \exp(-r)]^N , \quad (1)$$

where r is the normalized height of the peak power, and N is the number of independent frequencies. As noted by Scargle (1982), the oversampling is effectively interpolation and so does not increase the number of independent frequencies. This calculation of the FAP takes into account the number of independent frequencies that are searched for and corrects for the oversampling of the power spectra, but does not include the effect of searching for periodicity in multiple sources. When we are examining a power spectrum for the presence of a previously reported periodicity with a small uncertainty, N may be set equal to unity, and hence a signal with a lower amplitude can give a lower FAP than the case for a blind search. The uncertainty in the frequency of a candidate modulation that is detected can be calculated using the derivation of Horne & Baliunas (1986) that was also discussed by Levine et al. (2011),

$$\delta f = \frac{3}{8}\frac{1}{T\sqrt{r}} \quad (2)$$

.

Since the period, P, $= 1/f$, propagation of errors yields

$$\begin{aligned} \frac{\delta f}{f} &= \frac{\delta P}{P} \\ \Rightarrow \delta P &= \frac{3}{8}\frac{P^2}{T\sqrt{r}} \end{aligned} \quad (3)$$

Hence, the fractional uncertainty of the frequency and period

$$\frac{\delta f}{f} = \frac{\delta P}{P} \propto f^{-1}, \quad (4)$$

i.e., the fractional uncertainty on the measurement of the frequency and period of a detected modulation is smaller for short periods/high frequencies than for long periods/low frequencies. In addition, the degree to which a frequency can be measured more precisely than the intrinsic Fourier resolution, $\pm 1/(2T)$, scales as the square root of the normalized peak height. Hence, after a significant peak in the power spectrum has been detected, it is necessary to calculate the power spectrum in the vicinity of the peak with an oversampling ratio significantly $> 8/3\sqrt{r}$ to determine the frequency to better than the uncertainty implied by Equation (2). We typically choose to oversample by a factor of 20 greater than this, i.e., $\sim 50\sqrt{r}$.

In our photometric analyses, the background is not fitted for each time bin, and artifact signals can be seen at several periods, including Fermi's $\sim$90-minute orbital period, the survey period at twice this, one day, the Moon's 27.3-day sidereal period, the 53-day precession period of the Fermi satellite's orbit, and one quarter of a year related to the shape of the LAT point-spread function (PSF).[13]

Table 1
Swift-XRT Observations of 4FGL J1702.7−5655

Observation Start (UT Date)	Observation End (UT Date)	Exposure (s)
2011-11-01 19:58	2011-11-01 21:50	1220
2012-06-26 05:06	2012-06-26 05:12	280
2012-10-30 21:20	2012-10-30 21:36	810
2012-11-06 19:54	2012-11-06 20:16	915
2016-11-04 11:51	2016-11-04 19:55	1935
2021-02-06 02:13	2021-02-06 23:20	4435
2021-02-15 01:51	2021-02-16 22:28	1145
2021-03-03 00:00	2021-03-03 05:01	1385
2021-03-04 03:11	2021-03-04 22:28	5535

Note. The line indicates the division between Part 1 and Part 2 of the LAT light curve (MJD 56,345 = 2013-02-22).

2.2. X-Ray Observations and Analysis

The Swift-XRT (Burrows et al. 2005) is a Wolter I X-ray imaging telescope sensitive to X-rays ranging from 0.3 to 10 keV. The location of 4FGL J1702.7−5655 had previously been observed for 4 ks with the XRT under the program of Stroh & Falcone (2013) to monitor unassociated LAT sources. As no source was clearly detected in these observations, additional observations were obtained under the Swift TOO program to acquire a total exposure of $\sim$17.5 ks. All observations were made in photon-counting (PC) mode. The log of XRT observations is given in Table 1. We analyzed the existing and new data sets together using the online tools provided at the University of Leicester (Goad et al. 2007; Evans et al. 2009) to extract an image, and to detect the source and determine the position.[14]

2.3. Radio Observations and Analysis

Radio observations covering the location of 4FGL J1702.7−5655 were obtained using ATCA (Wilson et al. 2011) between December 2020 to November 2021 (MJD 59,208 to 59,540, see Table 2), i.e., during Part 2 of the gamma-ray light curve (Section 3.1), with observations centered at 2.1, 5.5, and 9.0 GHz, with 2 GHz bandwidths for all three bands. The ATCA, which consists of six antennas with 22 m diameter, was in several different array configurations over this period, with the more compact arrays somewhat more sensitive to the bright extended emission in the vicinity. Details of the array configurations are given in Table 2. Observations were reduced following standard procedures in Miriad (Sault et al. 1995). PKS 1657-56 was used as a phase calibrator, and PKS 1934-638 was used as a primary flux density calibrator for all observations.

[13] http://fermi.gsfc.nasa.gov/ssc/data/analysis/LAT_caveats_temporal.html
[14] https://www.swift.ac.uk/user_objects/

Table 2
Australia Telescope Compact Array Radio Observations of 4FGL J1702.7−5655

Observation Start (UT Date)	MJD	Configuration	Center Frequency (GHz)	Duration (minutes)
2020 Dec 25	59208	1.5A	2.1	541.1
2021 Jan 07	59221	1.5A	2.1	759.3
2021 Jan 14	59228	EW352	2.1	308.7
2021 Jan 16	59230	EW352	2.1	778.6
2021 Nov 22	59540	6C	5.5/9.0	68.9

Note. The first four observations used $17^h02^m46\overset{s}{.}68$, $-56°55'41\overset{''}{.}88$ as the target position, while the last used $17^h02^m51\overset{s}{.}45$, $-56°55'09\overset{''}{.}69$. The ATCA array configurations are the standard names for the physical locations of the antennas: see https://www.narrabri.atnf.csiro.au/operations/array_configurations/configurations.html for full details of the antenna spacings in each array configuration.

3. Results

3.1. Gamma-ray Results

From our examination of the power spectra of the LAT light curves of all 4FGL DR2 sources, we noted significant modulation from 4FGL J1702.7−5655. The power spectrum of the LAT light curve is shown in Figure 1. There is a prominent peak near a period of 0.24 days at a height of 25.7 times the mean power level of 1.3×10^{-19} (p .ph cm^{-2} s^{-1})^2, and the implied FAP is 7×10^{-7}. To investigate the frequency dependence of the continuum power, we performed a fit of the logarithm of the power as a function of the logarithm of the frequency, as advocated by Vaughan (2005). From this, we find that the continuum is very flat with only a hint of a small increase at lower frequencies/longer periods with $Power \propto f^{-4(\pm 2)\times 10^{-3}}$. We also calculated the mean power level around the peak in the period range 0.24 to 0.25 days, and the peak has a relative height of 24.5, which gives an FAP of 2.2×10^{-6}, calculated using the total number of independent frequencies for the full period range. We note that the apparent increase in power at shorter periods in Figure 1 is not real and is due to the logarithmic scale, which prevents individual points being discerned at high frequencies (f), and only the statistical envelope is visible.

No obvious peaks are seen at the second, third, or fourth harmonics of this. The period is determined to be 0.2438033 (11) days using the formulation of Horne & Baliunas (1986), i.e., 5.851279(26) hr. Since this would be a typical orbital period for a binary MSP (e.g., Papitto & de Martino 2022), we assume that this is indeed the orbital period of 4FGL J1702.7−5655. The probability-weighted aperture-photometry LAT light curve folded on the 0.24 day period is shown in Figure 2. This shows a relatively sharp dip that is strongly suggestive of the presence of an eclipse, implying that the system is observed at a high inclination angle.

In order to search for any long-term changes in the orbital modulation, we obtained a dynamic power spectrum of the probability-weighted aperture-photometry LAT light curve. We calculated power spectra for light curves with a length of 650 days, with offsets of 50 days between successive light curves. The results of this are shown in Figure 3, and it suggests that the orbital modulation was less apparent during earlier time ranges. To explore this further, we investigated the growth in relative height of the peak in the power spectrum as a function of time. For a persistent coherent signal with constant background and no other changes, the relative power should grow linearly with time because the amplitude noise decreases as the square root of the observation time. In Figure 4 we plot the relative height of the orbital peak using light curves that all end at the same time (MJD 59,445), but have different start dates. From this, it can be seen that as the start date is moved earlier, the relative strength of the peak initially grows as the light-curve length increases. However, for light-curve start times earlier than ∼3100 days before the end of the light curve (i.e., start times earlier than ∼MJD 56,345 = 2013-02-22), a plateau appears with little overall increase in relative power.

To investigate this in more detail, we calculated power spectra for the LAT light curve divided into two sections before and after MJD 56,345. These are shown in Figure 5, and it can be seen that there is no significant orbital peak in the power spectrum for the earlier light-curve segment (Part 1), while it is

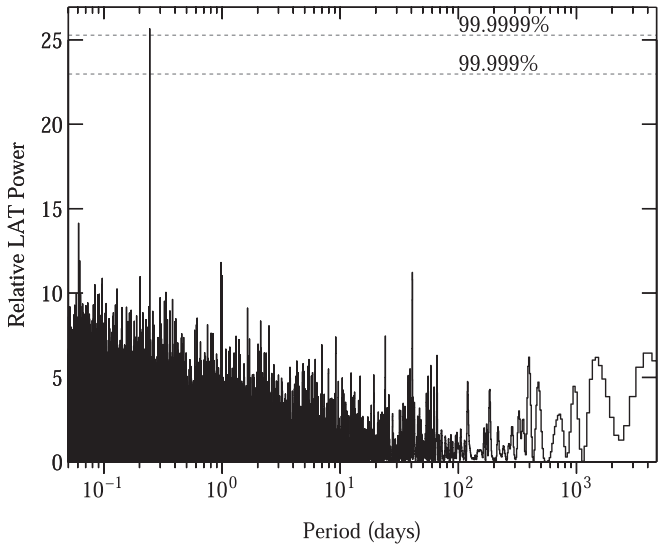

Figure 1. Power spectrum of the Fermi LAT probability-weighted aperture-photometry light curve of 4FGL J1702.7−5655. The power spectrum is normalized to the mean power level of 1.3×10^{-19} (p .ph cm^{-2} s^{-1})^2.

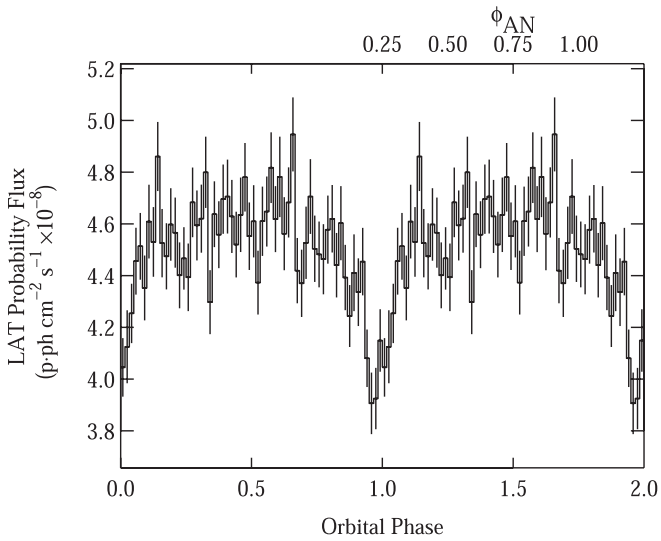

Figure 2. Fermi LAT probability-weighted aperture-photometry light curve of 4FGL J1702.7−5655 folded on the proposed orbital period. The bottom *X*-axis uses the eclipse center to define orbital phase zero. The upper labels show the predicted orbital phase with the time of the ascending node defining zero.

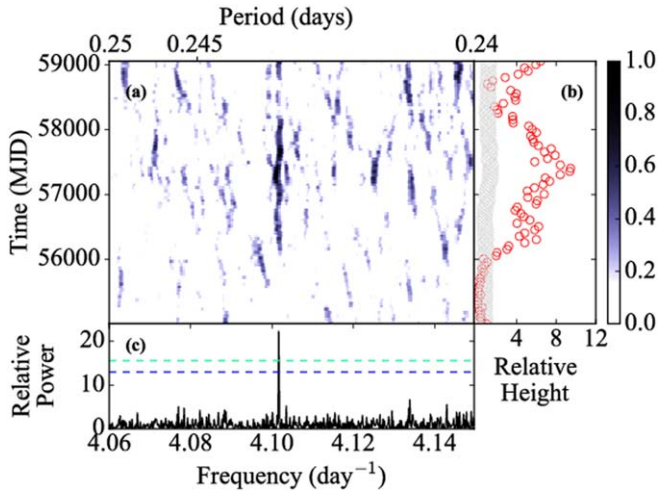

Figure 3. (a) Dynamic power spectrum of the probability-weighted aperture-photometry LAT light curve of 4FGL J1702.7−5655. (b) Relative peak at the orbital period to the mean power of the values shown in panel (a). (c) Coherent power spectrum of the entire light curve.

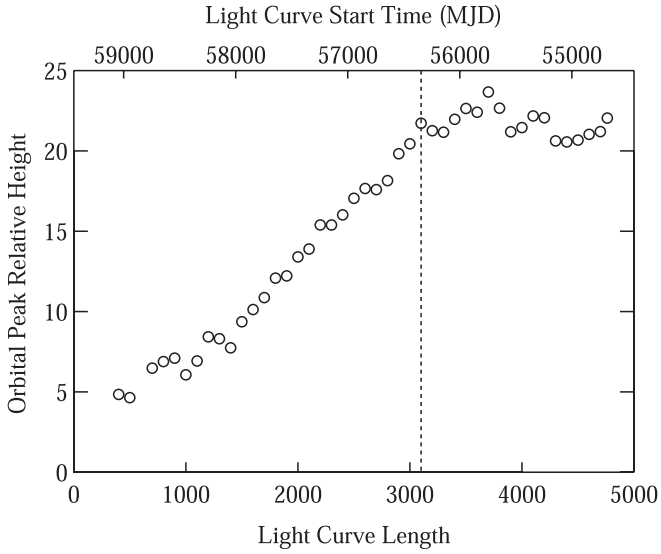

Figure 4. Relative height of the orbital peak in the power spectrum of the probability-weighted aperture-photometry LAT light curve of 4FGL J1702.7 −5655. All light curves have the same end date of MJD 54,682, and the start date, shown in the top axis, is changed in the analysis.

strongly detected for the later segment (Part 2). We then folded the light curve on the orbital period using data from these two time ranges, and they are shown in Figure 6. They show that the time of the minimum is shifted to the right and is broader for Part 2 compared to Part 1. In Part 2, the weighted count rate outside the eclipse is also slightly higher, as indicated by the upper panel of Figure 6, which shows the ratio of the two folded light curves.

We note that we cannot determine the exact time of the change in orbital modulation due to the long integration times required to detect the modulation and changes in it. We also investigated the effect on the power spectrum of dividing the light curve into halves with a split 600 days earlier (MJD 55,745), where the relative peak in Figure 4 is at its maximum. In this case, we find that the absolute power for Part 2 is reduced by ∼12% compared to dividing the light curve at MJD 56,345 (Figure 5). Thus, any sinusoidal orbital modulation between MJD 55,745 to 56,345 would be at a lower amplitude.

In order to search for other long-term changes in the gamma-ray properties that, for example, could be an indication of a state change in a tMSP, we calculated a light curve using a binned likelihood analysis. We performed likelihood fitting using time bins of 200 days, an energy range of 100 MeV to 500 GeV, a region of interest of 10°, and the spectral parameters for 4FGL J1702.7−5655 were allowed to float, while spectral values for other sources in the region were held fixed. The spectral model used for 4FGL J1702.7−5655 in the 4FGL catalog is a log normal function (`LogParabola`), i.e.,

$$\frac{dN}{dE} = K\left(\frac{E}{E_0}\right)^{-\alpha-\beta\, log_e(E/E_0)} \quad (5)$$

This model is used in the LAT catalogs for all sources with significantly curved spectra. The resulting light curve is shown in Figure 7, and the approximate time at which the orbital modulation changed to become prominent in the light curve is marked. Although the light curve is formally inconsistent with the hypothesis of being constant (χ^2_ν=3.1), we do not see any clear changes in the flux level or spectral parameters associated with the

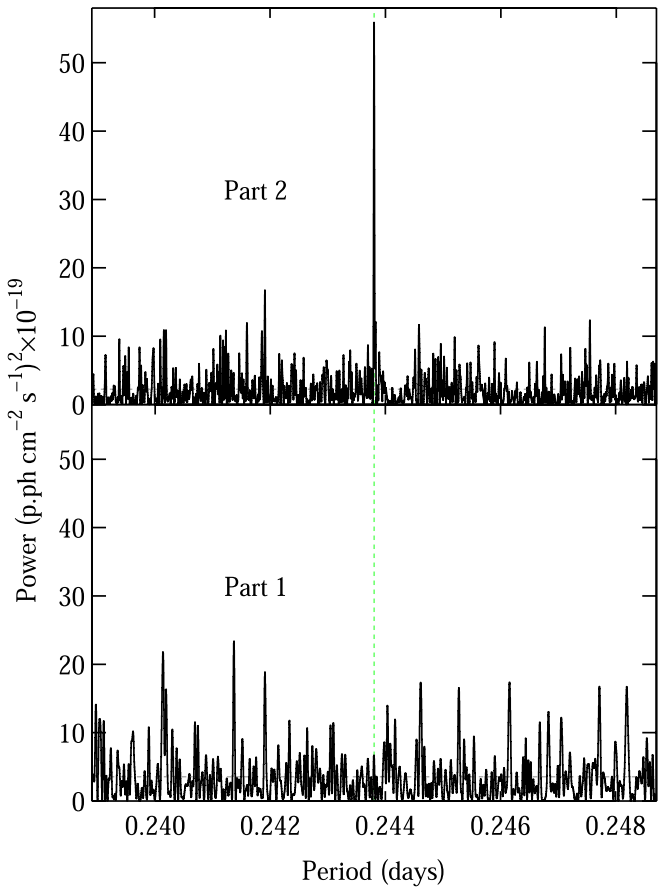

Figure 5. Power spectra of the probability-weighted aperture-photometry LAT light curve of 4FGL J1702.7−5655 obtained for time ranges of MJD 54,682-56,345 (bottom) and 56,345-59,445 (top). The period ranges are centered on the presumed orbital period marked with the vertical dashed green line. The mean power level for each panel is marked with a dashed horizontal gray line. Note that the *y*-axis is in units of absolute, rather than relative, power and that the same range is plotted for both panels.

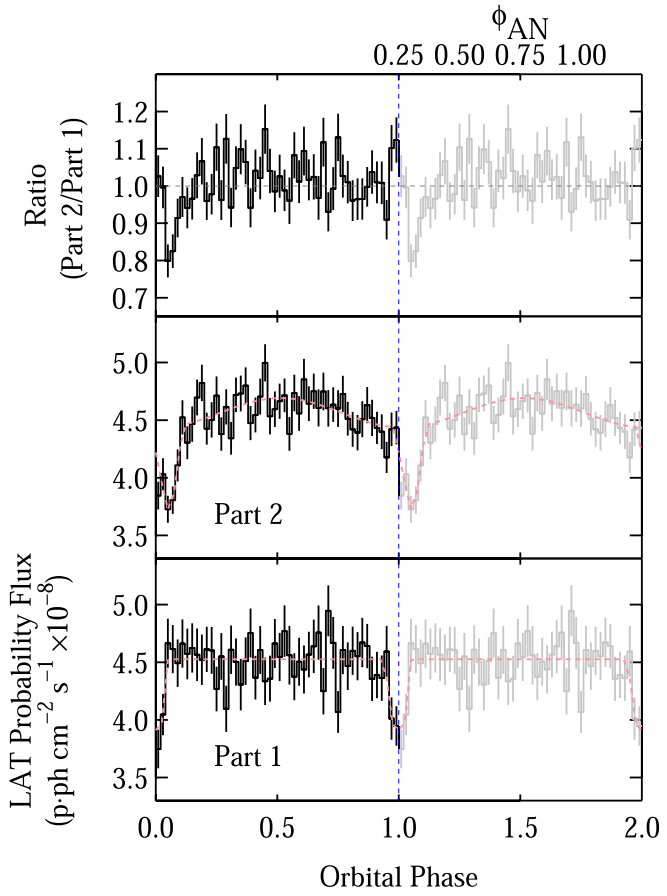

Figure 6. The probability-weighted aperture-photometry LAT light curve of 4FGL J1702.7−5655 obtained for time ranges of MJD 54,682-56,345 (bottom) and 56,345-59,445 (middle) folded on the orbital period. The top panel shows the ratio of the count rate in the second part to the first part. The dashed pink lines in the bottom two panels indicate the fits made to the unfolded light curves, and the parameters are given in Table 3. For clarity, two identical cycles are plotted for all panels, and the second cycle is plotted in gray. The bottom *X*-axis uses the eclipse center to define orbital phase zero. The upper labels show the predicted orbital phases with the time of ascending node defining zero.

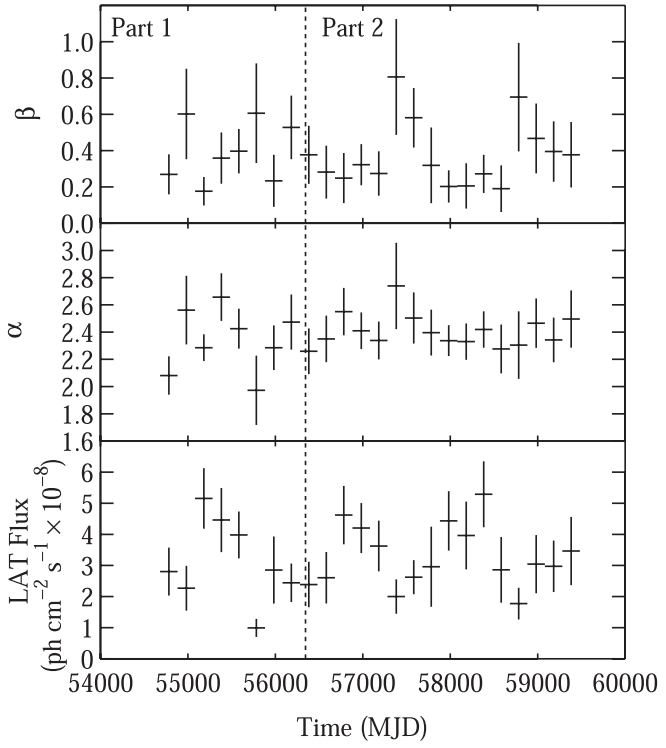

Figure 7. Long-term Fermi LAT light curve of 4FGL J1702.7−5655 obtained from a maximum likelihood analysis. The energy range is 100 MeV to 500 GeV, and the spectral parameters are for the logParabola model used in the 4FGL catalog. The dashed line shows the division between Part 1 and Part 2 at MJD 56,345.

change in the orbital profile. The mean flux before the division is $2.5 \pm 0.3 \times 10^{-8}$ ph cm^{-2} s^{-1} ($1.8 \pm 0.2 \times 10^{-11}$ erg cm^{-2} s^{-1}), while after it, it is $2.9 \pm 0.3 \times 10^{-8}$ ph cm^{-2} s^{-1} ($2.1 \pm 0.2 \times 10^{-11}$ erg cm^{-2} s^{-1}). For α, the values before and after are 2.36 ± 0.03 and 2.38 ± 0.3, while for β, they are 0.30 ± 0.05 and 0.30 ± 0.04, respectively.

In order to characterize the orbital modulation we fitted periodic functions to the unfolded weighted aperture-photometry light curves. Since the eclipse has a relatively short duration, we extracted light curves with 100 s time bins, i.e., ∼0.005 of the orbital period. We fitted the two parts of the light curve separately. For Part 1, we used an eclipse profile with constant fluxes outside and inside the eclipse, and linear transitions between them, with independent durations for the eclipse ingress and egress. The profile is defined in terms of orbital period (which is held fixed at the value found from the power spectrum) and time of eclipse center (T_0), which we define as $\phi = 0$, the phase of the start of eclipse ingress ($\phi_{\rm ing}$), the phase of the end of egress ($\phi_{\rm egr}$), the total duration of the eclipse minimum (Δ), flux outside the eclipse ($F_{\rm unecl}$), and flux during eclipse totality ($F_{\rm ecl}$). In the fits, $\phi_{\rm ing}$ and $\phi_{\rm egr}$ were constrained to occur before and after the phases of eclipse totality, respectively. Similarly to the computation of the power spectra, the data points were weighted by their relative exposures,

$$F = \begin{cases} F_{\rm unecl},\ \phi_{\rm egr} \leqslant \phi \leqslant \phi_{\rm ing} \\ F_{\rm unecl} + \left(\frac{(F_{\rm ecl} - F_{\rm unecl})(\phi - \phi_{\rm ing})}{\left(1 - \left(\frac{\Delta}{2}\right) - \phi_{\rm ing}\right)} \right),\ \phi_{\rm ing} \leqslant \phi \leqslant \left(1 - \left(\frac{\Delta}{2}\right)\right) \\ F_{\rm ecl},\ \phi \geqslant \left(1 - \left(\frac{\Delta}{2}\right)\right);\ \phi \leqslant \Delta/2 \\ F_{\rm ecl} + \left(\frac{(F_{\rm unecl} - F_{\rm ecl})\left(\phi - \left(\frac{\Delta}{2}\right)\right)}{\left(\phi_{\rm egr} - \left(\frac{\Delta}{2}\right)\right)} \right),\ \left(\frac{\Delta}{2}\right) \leqslant \phi \leqslant \phi_{\rm egr} \end{cases} \quad (6)$$

.

Derived from these fitted parameters are the total eclipse phase duration from eclipse ingress start to egress end ($1 + \phi_{\rm egr} - \phi_{\rm ing}$), the phase duration of the ingress $\left(1 - \left(\frac{\Delta}{2}\right) - \phi_{\rm ing}\right)$, and the phase duration of the egress $\left(\phi_{\rm egr} - \left(\frac{\Delta}{2}\right)\right)$.

For the fit to the unfolded Part 2 light curve, we used a sum of the same eclipse model together with an additional sine wave component. For both fits, we held the orbital period at the value determined from the power spectrum of Part 2. When we allowed the orbital period to be free, we found that this resulted in unstable fits.

The parameters from the fits to both sections of the light curve are given in Table 3. The parameter 1σ uncertainties are

Table 3
Fits to the Periodic Modulation of the LAT Light Curve of 4FGL J1702.7−5655

Parameter	Part 1	Part 2
Flux Outside Eclipse ($F_{\rm unecl}$)	4.53 ± 0.03	4.56 ± 0.02
Flux in Eclipse ($F_{\rm ecl}$)	3.91 ± 0.22	3.85 ± 0.15
Eclipse Center (T_0, MJD)	57000.168 ± 0.004	57000.181 ± 0.002
Eclipse Minimum Full Duration (Δ)	0.044 ± 0.038	0.021 ± 0.027
Eclipse Ingress Start ($\phi_{\rm ing}$)	0.940 ± 0.033	0.923 ± 0.021
Eclipse Egress End ($\phi_{\rm egr}$)	0.050 ± 0.019	0.055 ± 0.017
Eclipse Total Duration (Egress - Ingress) (ϕ)	*0.110 ± 0.038*	*0.132 ± 0.027*
Derived Ingress Duration (ϕ)	*0.038 ± 0.038*	*0.066 ± 0.024*
Derived Egress Duration (ϕ)	*0.028 ± 0.027*	*0.044 ± 0.022*
Sine Wave Half-amplitude	⋯	0.127 ± 0.034
Sine Wave Maximum (MJD)	⋯	57000.293 ± 0.009
Sine Wave Maximum[a] (ϕ)	⋯	*0.51 ± 0.04*
Sine Wave Maximum[b] (ϕ)	⋯	*0.46 ± 0.04*
χ^2_ν	0.78	1.04
Period (d)	*0.2438034*	*0.2438034*

Notes. Fits were made to the probability-weighted aperture-photometry light curve with 100 s time bins. Phase 0 corresponds to the center of the full eclipse. Parameters in italics are derived from the other parameters that were fitted. The orbital period was held fixed at the value determined from the power spectrum. Fluxes are in units of p.ph $\times 10^{-8}$ cm^{-2} s^{-1}.
[a] Relative to the Part 1 eclipse center.
[b] Relative to the Part 2 eclipse center. Fits are plotted in Figure 6.

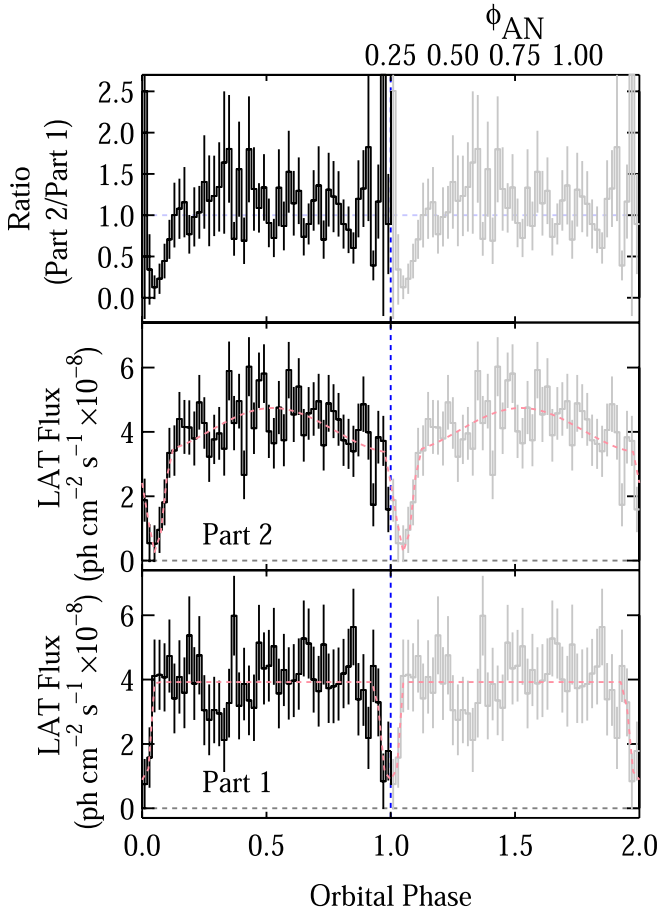

Figure 8. The binary phase-resolved flux of 4FGL J1702.7−5655 obtained from the likelihood analysis of LAT observations. Spectral parameters were held fixed at the 4FGL catalog (DR2) values. Fits are shown for time ranges of MJD 54,682-56,345 (bottom) and 56,345-59,445 (middle). The top panel shows the ratio of the fluxes in the second part to the first part. The dashed pink lines in the bottom two panels indicate the fits made to the folded light curves. The parameters are given in Table 4. For clarity, two identical cycles are plotted for all panels, and the second cycle is plotted in gray. The vertical dashed blue lines show the eclipse center as determined for Part 1. The bottom *X*-axis uses the eclipse center to define orbital phase zero. The upper labels show the predicted orbital phases with the time of ascending node defining zero.

derived from the intervals that give $\chi^2_{\rm min} + 1$ (Lampton et al. 1976; Yaqoob 1998).

We use the center of the eclipse for the Part 1 light curve to define phase zero and find this to be MJD 57,000.168, with an uncertainty of 0.004 days (uncertainty of 0.017 in phase). This would correspond to superior conjunction of a pulsar, assuming that is indeed the source of the gamma-rays and that it is being eclipsed by its companion. For a pulse-timing circular orbit with phase 0 defined as the ascending node, this would correspond to a phase ($\phi_{\rm AN}$) of 0.25. The Part 1 eclipse width from ingress start to egress end is 0.110 ± 0.038 in phase. The ingress and egress durations are not well defined and are consistent with 0.

For the Part 2 light curve, the center of the eclipse minimum is shifted to a slightly later time by 0.014 ± 0.005 days. i.e., our fits indicate that the centers of the two eclipses differ 0.059 ± 0.020 in phase. The semi-amplitude of the sine wave component is $0.127 \pm 0.034 \times 10^{-8}$ p.ph cm^{-2} s^{-1}, equivalent to a fractional semi-amplitude of $2.8 \pm 0.7\%$. This corresponds to a power of $16 \pm 9 \times 10^{-19}$(p.ph cm^{-2} s^{-1})^2. The measured power for the orbital modulation in Part 2 is $\sim 55 \times 10^{-19}$(p.ph cm^{-2} s^{-1})^2 (Figure 5), and so, at least in this representation of the light-curve components, the eclipse feature also contributes to the observed signal in the power spectrum. This may be due to the eclipse, which occurs at the minimum of the sine component, becoming broader. We note, however, that this mathematical deconvolution does not necessarily relate to two astrophysically distinct components.

We next investigated the orbital gamma-ray modulation by performing likelihood fits to binary phase-resolved LAT data. We divided the light curve into 50 phase bins. Our analysis was similar to that for the long-term light curve, except that we also held the spectral parameters of 4FGL J1702.7−5655 fixed and only allowed its flux to vary. The likelihood analysis was performed for the Part 1 and Part 2 light curves separately, and the resulting light curves and their ratios are shown in Figure 8. The folded light curves are similar in overall properties to the folded probability-weighted aperture-photometry light curves (Figure 2). However, it can now be seen that the minima during the eclipses are very close to zero flux, and given the uncertainties in the background, are consistent with zero. To characterize these phase-resolved likelihood light curves, we again fitted the same functions that we employed for the aperture-photometry light curves, i.e., an eclipse profile for Part 1, and an eclipse profile plus sine component for Part 2. We kept the eclipse time parameters (center time, phase duration, and phase of eclipse ingress and egress) held fixed at the values determined from fitting the aperture-photometry light curves and only allowed the fluxes and the phase of the sine wave to be free. The results are given in Table 4 and are overplotted on the light curves in Figure 2. In this parameterization, the

Table 4
Fits to the Binary Phase-resolved LAT Light Curve of 4FGL J1702.7−5655

Parameter	Part 1	Part 2
Flux Outside Eclipse ($F_{\rm unecl}$)	3.92 ± 0.16	4.04 ± 0.12
Flux in Eclipse ($F_{\rm ecl}$)	0.89 ± 0.48	0.96 ± 0.44
Sine Wave Half-amplitude	⋯	0.70 ± 0.18
Sine Wave Maximum (MJD)	⋯	*57000.296 ± 0.009*
Sine Wave Maximum[a] (ϕ)	⋯	0.52 ± 0.04
Sine Wave Maximum[b] (ϕ)	⋯	*0.47 ± 0.04*
χ^2_ν	0.58	0.997
Period (d)	*0.2438034*	*0.2438034*

Notes. Fits were made to the phase-resolved fluxes obtained from likelihood analysis. Eclipse parameters, excluding flux, were held fixed at the values obtained from fitting the aperture-photometry light curve given in Table 3. Parameters in italics are derived from the other parameters that were fitted. Fluxes are in units of ph$\times 10^{-8}$ cm^{-2} s^{-1}.
[a] Relative to the Part 1 eclipse center.
[b] Relative to the Part 2 eclipse center. The fits are plotted in Figure 8.

out-of-eclipse fluxes are consistent with being the same for both Part 1 and Part 2. The maximum of the sine wave component is again found to be 0.5 in phase away from the eclipse, i.e., at inferior conjunction. The sine wave semi-amplitude is $17 \pm 4\%$ of the out-of-eclipse flux. We note that the difference between the mean out-of-eclipse flux and the flux at eclipse minimum of $(3.1 \pm 0.5) \times 10^{-8}$ ph cm^{-2} s^{-1} significantly exceeds the sine wave semi-amplitude of $(0.70 \pm 0.18) \times 10^{-8}$ ph cm^{-2} s^{-1}.

3.2. X-Ray Results

A smoothed image obtained from the Swift-XRT observations is shown in Figure 9. We find that there is an excess within the Fermi 68% error ellipse at $17^{\rm h}02^{\rm m}51\overset{\rm s}{.}01$, $-56°55'09\overset{''}{.}1$ with an uncertainty of $4\overset{''}{.}2$. The detection signal-to-noise ratio is 3.7 with 34 counts compared to an expected background of 10. Due to the small number of counts, it is not possible to obtain a spectrum of this candidate source. Of the total ∼17.5 ks XRT exposure time, only ∼3 ks was obtained during Part 1 of the light curve, which also hampers an investigation of any change in X-ray flux associated with the change in the gamma-ray orbital modulation. In Figure 10 we show the Deep Sky Survey 2 red image centered on the XRT location. Within the error region are several stars that are blended in this image. Optical spectroscopy of these stars is in process and will be published later (S. J. Swihart et al. 2022, in preparation).

3.3. Radio Results

Although several radio sources were detected within the ATCA field of view, none lie within the LAT error region. Hence, we are only able to obtain upper limits on the presence of a radio counterpart. From the summed images at each frequency, we obtain 3σ upper limits at the source location of 66, 69, and 69 μJy at 2.1, 5.5, and 9.5 GHz, respectively. We note that in the second Fermi LAT catalog of gamma-ray pulsars (2PC; Abdo et al. 2013), sources with flux densities <30 μJy at 1.4 GHz are regarded as radio quiet, and that most pulsars have spectral indices of −1.7. Thus, at ∼2 GHz radio-quiet sources would have flux densities $\lesssim 60$ μJy, which is comparable to our upper limits, and hence we cannot yet exclude the presence of a radio pulsar.

4. Discussion

4.1. The Characteristics of the Orbital Modulation in 4FGL J1702.7−5655

The sharp dip seen in both the earlier and later portions of the light curve is consistent with an eclipse of the gamma-ray emitting region by a companion star in a highly inclined orbit. This is thus consistent with the proposed classification as a redback system. The presence of strong modulation seen in the power spectrum of the LAT light curve is exceptional for binary MSPs. The detection of the period is related to the change in orbital modulation. When tMSPs undergo state changes, flux variations (e.g., Roy et al. 2015) larger than the somewhat modest change in orbital profile seen for 4FGL J1702.7−5655 are observed, which are not accompanied by large changes in the gamma-ray flux or spectrum.

We next review orbital modulation in other binary MSPs as previously reported from LAT observations for comparison with 4FGL J1702.7−5655. For several systems, we also consider the properties of this modulation as found from our program. The parameters of these systems are summarized in Table 5. For 4FGL J1702.7−5655, we have used the center of the eclipse to define orbital phase 0. For most systems discussed here, pulse-timing orbits have been derived, but no eclipses have been observed. Hence, for these systems, the time of the ascending node is typically used to define orbital phase ($\phi_{\rm AN}$) 0. For a circular orbit where the gamma-ray emission is centered on the neutron star, the ascending node will occur 0.25 in phase earlier than an eclipse, i.e., an eclipse would be expected to occur at superior conjunction of the pulsar at $\phi_{\rm AN} = 0.25$, and inferior conjunction of the pulsar (compact object nearest us) would occur at $\phi_{\rm AN} = 0.75$.

4.2. Comparison with Orbital Modulation of Gamma-Ray Emission in Other Systems

4.2.1. Other Eclipsing MSP Systems

To investigate whether any of the other known gamma-ray eclipsing MSP systems (Strader et al. 2016; Kennedy et al. 2020; Clark et al. 2021b) also show any quasi-sinusoidal modulation, which could be a sign that such modulation depends on the inclination angle of a system, we calculated the power spectra of the LAT light curves of these sources around their orbital periods. They are plotted in Figure 11. For no other eclipsing system is the orbital period detectable in the power spectrum, although we note that these systems are all fainter than 4FGL J1702.7−5655 (Table 5). For PSR B1957+20, we note that Wu et al. (2012) reported orbital modulation of >2.7 GeV gamma-rays from Fermi LAT observations with a maximum near the phase of radio eclipse, i.e., pulsar superior conjunction at $\phi_{\rm AN}$ ∼0.25. We also calculated a probability-weighted aperture-photometry light curve for 4FGL J1959.5+2048 (PSR B1957+20) for energies above 2.7 GeV. However, the power spectrum of this does not show any modulation at the orbital period, and folding the light curve on the orbital period did not reveal orbital modulation either.

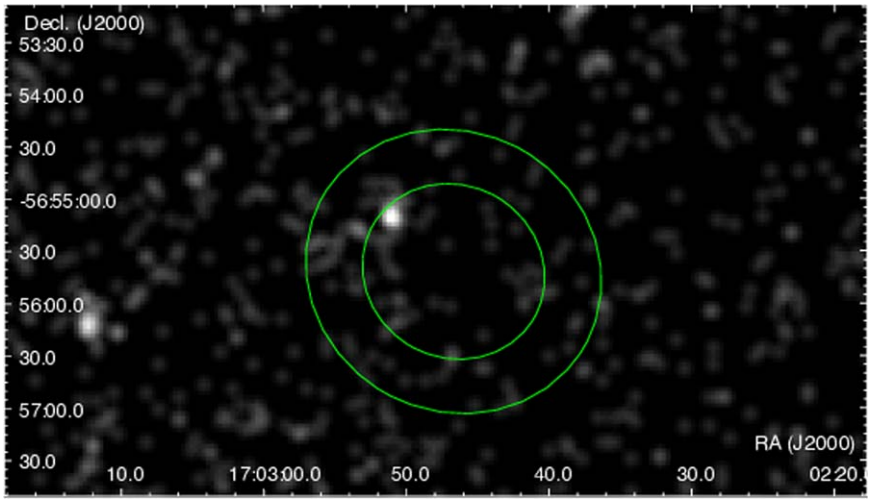

Figure 9. Smoothed Swift-XRT image of the region around 4FGL J1702.7−5655. LAT 68% and 95% confidence regions are marked. The candidate X-ray counterpart is the brightest source within the 68% region.

4.2.2. 4FGL J2039.5-5617 (PSR J2039−5617)

The redback system 4FGL J2039.5-5617 (=PSR J2039 −5617, 3FGL 2039.6-5618, "J2039.5") was found to have its gamma-ray emission as measured with the LAT modulated on its 0.228-day orbital period with an approximately sinusoidal profile by Ng et al. (2018). The phasing of the gamma-ray modulation in J2039.5 is that it has a maximum at $\phi_{\rm AN} = 0.25 \pm 0.03$ (Clark et al. 2021a), i.e., superior conjunction. The maximum of the sinusoidal modulation in 4FGL J1702.7−5655 is thus 0.5 out of phase with that in J2039.5, if the eclipse is indeed that of the compact object in the system. Ng et al. (2018) suggested that the amplitude of the orbital modulation had decreased after ∼MJD 57,000. Such a change in the sinusoidal modulation could indicate a similarity with 4FGL J1702.7−5655. Clark et al. (2021a) subsequently detected gamma-ray pulsations using the LAT at a period of 2.65 ms. However, Clark et al. (2021a) found that the orbital modulation increased again after MJD 58,100 and suggested that this could be due to statistical variations rather than intrinsic changes in the source. Ng et al. (2018) and Clark et al. (2021a) noted that the time of apparent decrease in orbital modulation coincided with an outburst from the blazar candidate 4FGL J2052.2−5533 (3FGL J2051.8–5535), which lies only 1.°9 from J2039.5 and experienced a flare around ∼56,500 to 57,500.

Our power spectrum of the LAT light curve of J2039.5 is shown in Figure 12. In the bottom panel, which covers the entire frequency range, the strongest peak is near one day, and this is a commonly seen artifact in the power spectra of LAT light curves. The second strongest peak is at a period of 2429 ± 112 days, and this long-period/low-frequency peak may be due to contamination from 4FGL J2052.2−5533. The third strongest peak is at the orbital period of J2039.5. The frequency range around this is plotted in the upper panel of Figure 12. The period we derive is 0.227978(1), consistent at the 1.8σ level with the period of 0.227979805(3) days found by Clark et al. (2021a) from pulse timing. The relative height of the peak is 17, which corresponds to an FAP of 0.004 (i.e., 99.6% significance) for a blind search over the entire frequency range, and 4×10^{-8} for a single-frequency trial. We note the presence of a peak almost as strong as the orbital modulation close to the orbital period at 0.225601(1) days. While Clark et al. (2021a) reported variations in the orbital period of J2039.5, these have a total range of $\Delta P/P \sim 10^{-6}$ and so would not result in the second peak with a period difference of ∼1%. We speculate that this peak is caused by aliasing, although it would be unclear how this is arising as the frequency difference between these nearby peaks corresponds to a period of ∼21.6 days. We note that J2039.5 is rather fainter than 4FGL J1702.7−5655, which can account for the lower relative height of the modulation in J2039.5 even if both sources had similar variability.

We next investigated the rate of change of the orbital peak in the power spectrum as a function of light-curve length in a similar way to our analysis of 4FGL J1702.7−5655. Consistent with Ng et al. (2018) and Clark et al. (2021a), we find a decrease in the rate of relative peak height change with light-curve length between approximately MJD 57,000 and 58,000. But we again cannot necessarily attribute this to a reduction in modulation strength as this coincides with the flare in 4FGL J2052.2−5533. To investigate further, we calculated power spectra for 1000-day-long time intervals, and these are show in Figure 13. We find that for segment (c), which covers MJD 57,000–58,000, modulation is not seen at the orbital period, although there is no large change in the continuum power level. This may suggest that during this time, the lack of a detection of orbital modulation may be caused by the reduced amplitude, and not just by an increase in the background noise level due to the AGN flare. Nevertheless, the temporal coincidence with this flare does hinder a unambiguous determination whether there was indeed a reduction in orbital gamma-ray modulation.

4.2.3. Quasi-sinusoidal Modulation of Pulsed Emission in 4FGL J2339.6−0533 (PSR J2339−0533)

The redback PSR J2339−0533 (4FGL J2339.6−0533, "J2239.6") shows quasi-sinusoidal modulation of the LAT flux on the ∼0.193-day orbital period (An et al. 2020). However, in this system it is the pulsed gamma-ray emission of the 2.9 ms pulsar that is orbitally modulated, which is difficult to explain. For J2239.6, the orbital maximum occurs near superior conjunction (when the neutron star is farthest from us), which is similar to J2039.5, but again apparently 0.5 out of phase with 4FGL J1702.7−5655. In J2239.6, similar to other binary MSPs for which orbital modulation has been claimed,

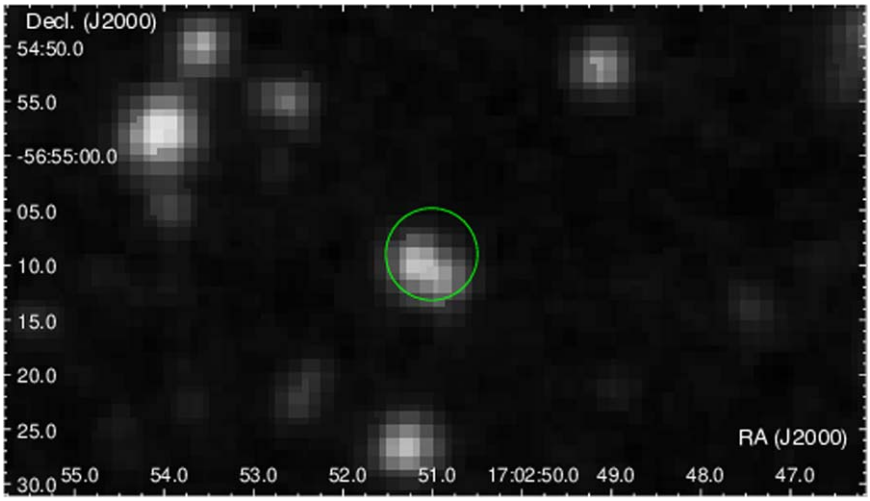

Figure 10. DSS2 red image of the region around the possible XRT counterpart of 4FGL J1702.7−5655. The XRT error region is marked.

Table 5
Selected Binary Millisecond Pulsars

Name	Photon Flux (ph cm^{-2} s^{-1} × 10^{-10})	Energy Flux (erg cm^{-2} s^{-1} × 10^{-12})	Orbital Period (days)	Pulse Period (ms)	Eclipse?	Sine?
4FGL J1702.7−5655	31.68 ± 1.10	29.09 ± 1.43	0.2438033	?	Y	Y/I(?)
4FGL J1048.6+2340 (PSR J1048+2339)	6.38 ± 0.53	5.07 ± 0.49	0.2505191 (a)	4.67	Y	N
4FGL J1816.5+4510 (PSR J1816+4510)	16.91 ± 0.74	10.18 ± 0.52	0.3608934817 (b)	3.19	Y	N
4FGL J0427.8−6704	6.57 ± 0.43	8.57 ± 0.49	0.3667200 (c)	?	Y	N
4FGL J1959.5+2048 (PSR B1957+20)	23.29 ± 1.1	16.07 ± 0.89	0.38196661 (d)	1.61	Y	Y/S
4FGL J2129.8−0428 (PSR J2129-0429)	11.51 ± 0.72	6.68 ± 0.49	0.63522741310 (e)	7.61	Y	N
4FGL J1311.7−3430 (PSR J1311−3430)	75.68 ± 1.50	60.97 ± 1.26	0.0651157347 (f)	2.56	N	Y/I
4FGL J2241.7−5236 (PSR J2241−5236)	46.82 ± 1.37	25.37 ± 1.11	0.1456722372 (g)	2.19	N	Y/S
4FGL J2339.6−0533 (PSR J2339−0533)	47.02 ± 1.26	29.16 ± 0.84	0.19309790 (h)	2.88	N	Y/S
4FGL J2039.5−5617 (PSR J2039−5617)	21.83 ± 0.83	15.13 ± 0.67	0.227979805 (i)	2.65	N	Y/S
4FGL J1228.0−4853 (PSR J1227−4853)	24.80 ± 1.08	22.58 ± 1.26	0.287887802 (j)	1.69	N	Y/S[a]

Note. Photon flux is for the energy range 1–100 GeV, energy flux is for the range 100 MeV to 100 GeV. Both are taken from the 4FGL DR2 catalog (v27). The "Eclipse" column indicates whether an eclipse has been reported in LAT observations. The "Sine" column indicates whether quasi-sinusoidal modulation in gamma-rays has been reported, where "S" and "I" indicate that orbital maximum is nearest superior or inferior conjunction of the compact object.
[a] For 4FGL J1228.0−4853 an orbital maximum was reported near inferior conjunction by Xing & Wang (2015), while An (2022) reported a minimum near that phase from a longer data set. References: (a) Deneva et al. (2016), (b) Stovall et al. (2014), (c) Kennedy et al. (2020), (d) Arzoumanian et al. (1994), (e) Kong et al. (2018), (f) An et al. (2017), (g) An et al. (2018), (h) Romani & Shaw (2011), (i) Clark et al. (2021a), (j) de Martino et al. (2020). The orbital period for 4FGL J1702.7−5655 is from this work.

the gamma-ray modulation was not found from a blind search, but relied on the orbital period already being known. For J2339.6, we do not detect significant modulation from our probability-weighted aperture-photometry light curve, consistent with the report by An et al. (2020) that orbital modulation is only present in the on-pulse.

4.2.4. The Transitional Source XSS J12270−4859 (4FGL J1228.0−4853)

XSS J12270−4859 (4FGL J1228.0−4853, PSR J1227−4853) is a transitioning redback that switched from an LMXB to an MSP state in 2012 (Bassa et al. 2014). An (2022) reported that the gamma-ray flux (60 MeV − 1GeV) was modulated on the ∼0.29-day orbital period of the system, with minimum at inferior conjunction of the orbit ($\phi_{AN} = 0.75$), and maximum near superior conjunction ($\phi_{AN} = 0.25$). Curiously, An (2022) found that the orbital gamma-ray modulation was similar in both the MSP and LMXB states. However, Xing & Wang (2015) had previously reported the presence of orbital modulation in LAT gamma-ray observations (>200 MeV) with a maximum near inferior conjunction ($\phi_{AN} = 0.75$) that was only seen after the transition to the MSP state.

To investigate the presence of orbital modulation in our 100 MeV–500 GeV light curve of 4FGL J1228.0−4853, we calculated power spectra for the time intervals before and after MJD 56,250 (2012 November 19), and they are shown in Figure 14. For the earlier time interval when XSS J12270-4859 was in an LMXB state, we do not detect orbital modulation. However, for the later time interval, when the source had transitioned to an MSP state, we see a peak at a period of 0.287888(3), consistent with the orbital period. The peak's relative height is 7.8, which corresponds to a single trial FAP of 4×10^{-4}. The detection of orbital modulation only in the MSP state is similar to the result of Xing & Wang (2015). However, the light curves for the same time intervals folded on the orbital

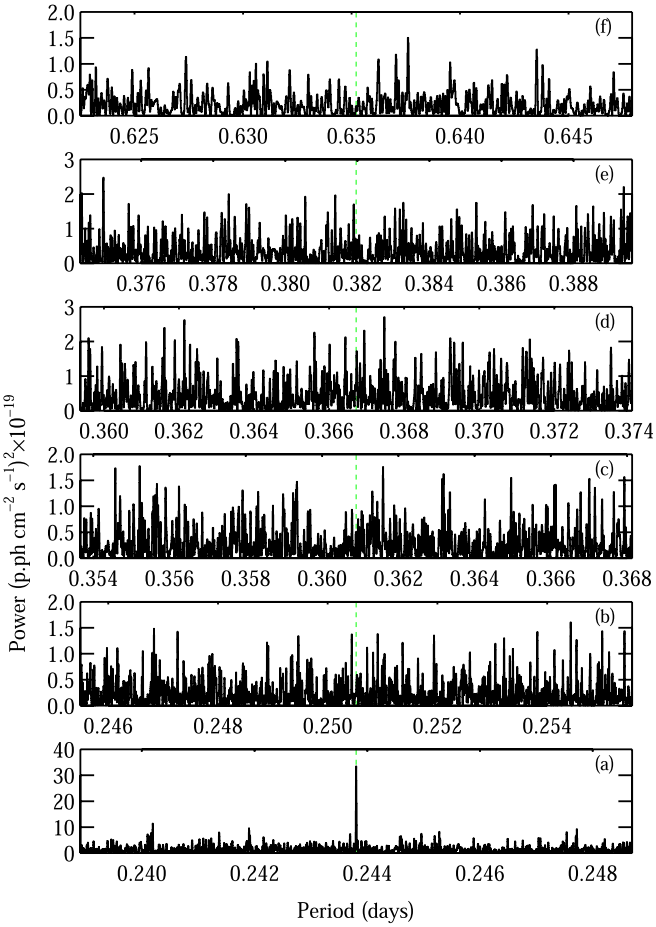

Figure 11. A comparison of the power spectrum of 4FGL J1702.7−5655 with the power spectra of probability-weighted aperture photometry for candidate redback systems for which eclipses have been reported and are present in the 4FGL DR2 catalog. Power spectra are centered on the orbital periods (Table 5), which are marked by the vertical dashed green line. (a) 4FGL J1702.7−5655, (b) 4FGL J1048.6+2340 (PSR J1048+2339), (c) 4FGL J1816.5+4510 (PSR J1816+4510), (d) 4FGL J0427.8−6704, (e) 4FGL J1959.5+2048 (PSR B1957 +20), (f) 4FGL J2129.8−0428 (PSR J2129−0429).

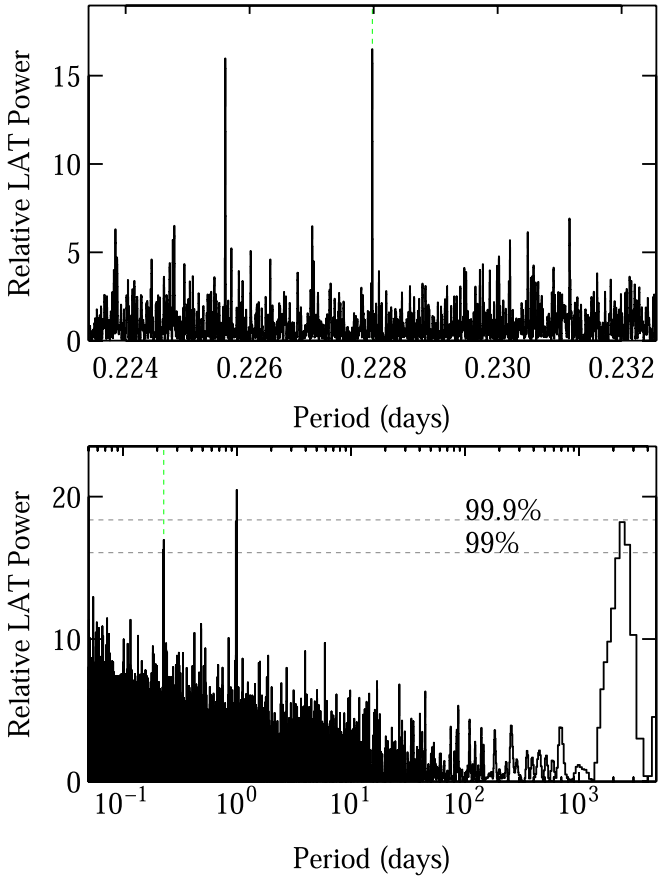

Figure 12. Power spectra of the probability-weighted aperture-photometry LAT light curve of 4FGL J2039.5−5617 (=PSR J2039−5617). The bottom panel shows a range from 0.05 days to the length of the light curve, while the top panel shows the detail around the orbital period of 4FGL J2039.5−5617, which is marked with dashed green lines in both panels. The peak near one day in the bottom panel is a common artifact seen in the power spectra of many LAT sources.

period (Figure 15) show that for the later time interval, the highest flux is at $\phi_{\rm AN}$∼0.25, similar to the result of An (2022).

4.2.5. The Black Widows PSR J1311−3430 and PSR J2241–5236

Orbital modulation in the off-pulse emission has also been reported for the black widow systems PSR J1311−3430 (4FGL J1311.7−3430, "J1311.7"; Xing & Wang 2015; An et al. 2017) and PSR J2241-5236 (4FGL J2241.7−5236, "J2241.7"; An et al. 2018). For J1311.7, the maximum occurs at $\phi_{\rm AN} = 0.8$, i.e., near inferior conjunction and minimum at $\phi_{\rm AN} = 0.4$. For J2241.7 maximum occurs at superior conjunction ($\phi_{\rm AN}$ 0.25) with a possible secondary maximum at $\phi_{\rm AN} = 0.75$.

While these systems did not appear in our blind search for periodicities, power spectra centered around the known periods do show an indication of modulation for J2241.7 (Figure 16). In the blind search over the full frequency range, this period is not readily detectable as its relative height is only ∼13 (FAP = 0.19), and it is the second highest peak after the one-day artifact. However, for a single trial, the FAP is $\sim 2 \times 10^{-6}$. No power spectrum peak is seen for J1311.7 (Figure 16)—for this source, we also investigated using shorter time bins of 100 s due to the short (0.065 day) orbital period, and no change to the power spectrum was found. Folding the aperture-photometry light curves on the known periods (Figure 17) does show modulation for both systems. The modulation is thus detectable in the overall emission from both systems without pulse-phase selection. For both sources, we see orbital maximum at the same phases as previously reported (An et al. 2017, 2018). There thus appears to be no large difference in the pulse-averaged profiles with the orbital profiles seen in the off-pulse emission, although the amplitudes are lower.

4.3. Implications for 4FGL J1702.7−5655

The gamma-ray variability in 4FGL J1702.7−5655 is characterized by two modes of periodic behavior. In Part 1 of the light curve, the only modulation that is clearly present is the rather sharp dip that reduces to a level consistent with the background. Then, this transitions to a combination of a dip in the light curve at a slightly later phase together with the appearance of quasi-sinusoidal modulation. This change in periodic behavior is not accompanied by a significant change in the overall gamma-ray brightness or spectral parameters. While some aspects of the variability of 4FGL J1702.7−5655 have been seen before in other sources, this combination of eclipses and transient (on timescales of years) quasi-sinusoidal modulation has not been reported previously.

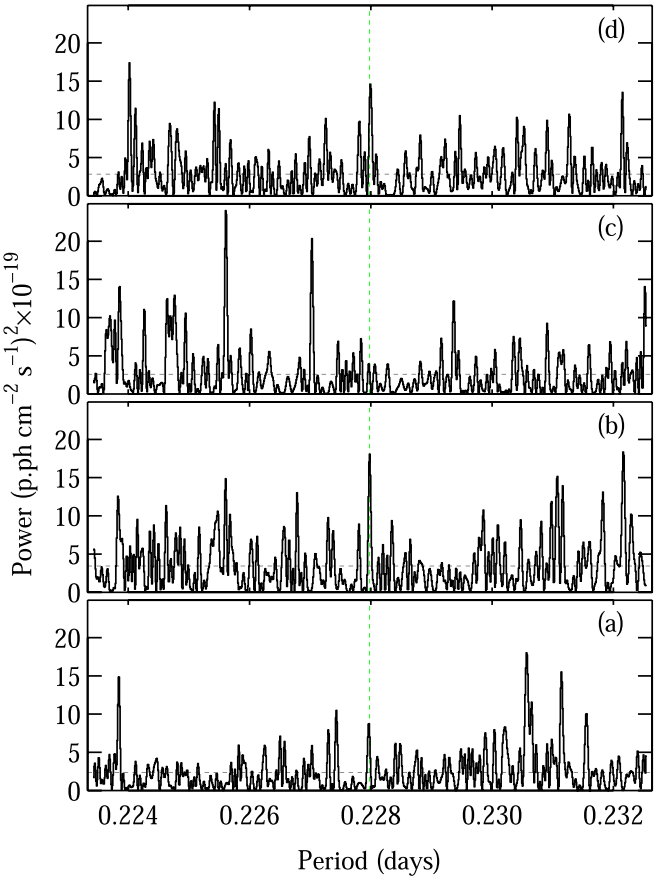

Figure 13. Power spectra of the probability-weighted aperture-photometry LAT light curve of 4FGL J2039.5−5617 (=PSR J2039−5617) divided into time segments: (a) MJD 55000-56000, (b) MJD 56,000-57,000, (c) MJD 57,000-58,000, and (d) MJD 58,000-59,000. The orbital period of 4FGL J2039.5−5617 is marked with dashed vertical green lines in all panels, and the dashed horizontal gray lines show the mean power levels.

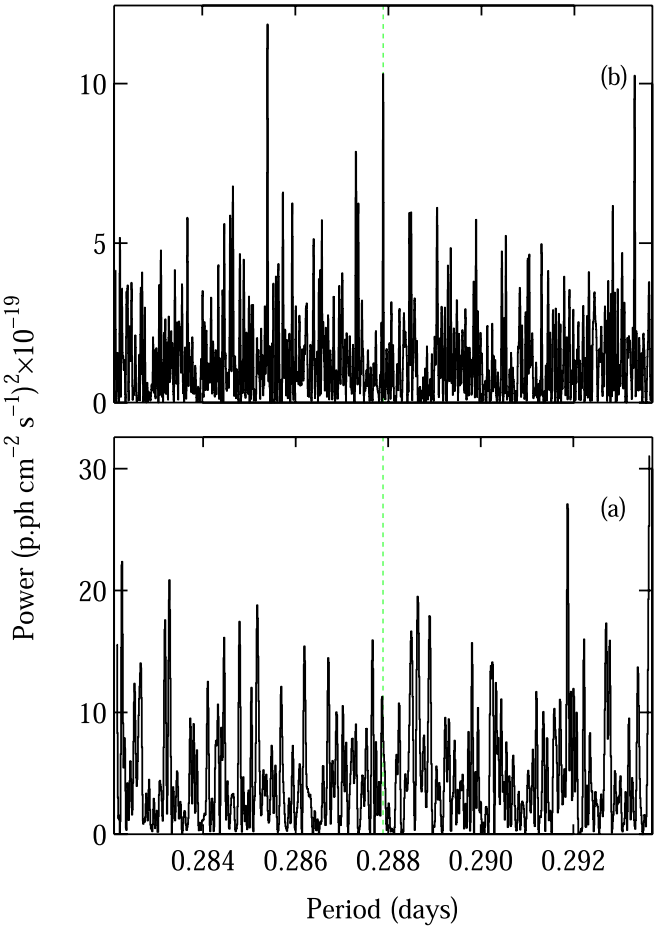

Figure 14. Power spectra of the probability-weighted aperture-photometry LAT light curves of the transitional MSP XSS J12270-4859 (4FGL J1228.0 −4853) for the time intervals of (a) MJD 54,682-56,250 and (b) MJD 56,250-59,445. The orbital period (Table 5) is marked by the dashed green lines.

The light-curve dip in Part 2 reaches a similarly low level to that during Part 1, which implies that the gamma-ray emitting region is still sufficiently small to be totally eclipsed. However, the minimum occurs later by ∼0.05 in phase. i.e., the gamma-ray emission region is trailing the previous center of emission by ∼15°. In addition, the gamma-ray emission now has a nonisotropic component, which results in quasi-sinusoidal orbital modulation with a semi-amplitude of $17 \pm 4\%$. Since pulsations have not yet been detected from 4FGL J1702.7 −5655, we cannot determine whether the orbital modulation in Part 2 is pulse-phase dependent.

The X-ray brightness of 4FGL J1702.7−5655 is low, which suggests that the system has not transitioned to an accreting LMXB state. While we do not yet have an accurate measurement of the X-ray spectrum or a distance to the source, we can make a rough estimate of the X-ray to gamma-ray flux (F_X/F_γ). At a count rate of $\sim 1.4 \times 10^{-3}$ cts s^{-1}, we adopt a power-law spectrum with a photon-index of 1.75 and $N_H = 1.25 \times 10^{21}$ cm^{-2} (HI4PI Collaboration et al. 2016). Using PIMMS[15], the unabsorbed 0.5–10 keV flux is 6×10^{-14} erg cm^{-2} s^{-1}. The ratio F_X/F_γ, using the LAT catalog 0.1–100 GeV flux (Table 5), is 0.002. Although this has considerable uncertainty, it is much lower than the values of ∼0.25-0.4 for tMSPs in the subluminous disk state reported by Miller et al. (2020). If the XRT source is not the counterpart of 4FGL J1702.7−5655, then the ratio of F_X/F_γ must be even lower. Nevertheless, even though 4FGL J1702.7−5655 apparently did not transition to an LMXB state, some type of change did occur in the system.

Although we do not yet have a Doppler orbit for 4FGL J1702.7−5655, it appears highly likely that the "eclipse" is indeed the superior conjunction of a pulsar (nondegenerate object nearest us). The short ingress and egress, and the minimum being consistent with zero flux, indicate an eclipse rather than a change in absorption or emission due to the changing system geometry. Were it not an eclipse, the inclination would have to be lower than about 80° given the orbital period and typical masses of such systems. The angle dependences of inverse Compton scattering, absorption due to pair production, or Doppler-boosted emission would then produce a smoother modulation and would be unlikely to produce zero flux. Given the greater penetrating power of gamma-rays compared to X-rays or radio waves, a much more substantial amount of material is required to cause significant absorption. Due to this, while radio and X-ray emission can be attenuated by winds, for example, to cause a ∼100% drop in gamma-rays requires the body of a star (e.g., Clark et al. 2021b).

For Part 1 of the light curve, where the orbital modulation is apparently less complicated, the total eclipse duration (ingress

[15] https://heasarc.gsfc.nasa.gov/cgi-bin/Tools/w3pimms/w3pimms.pl

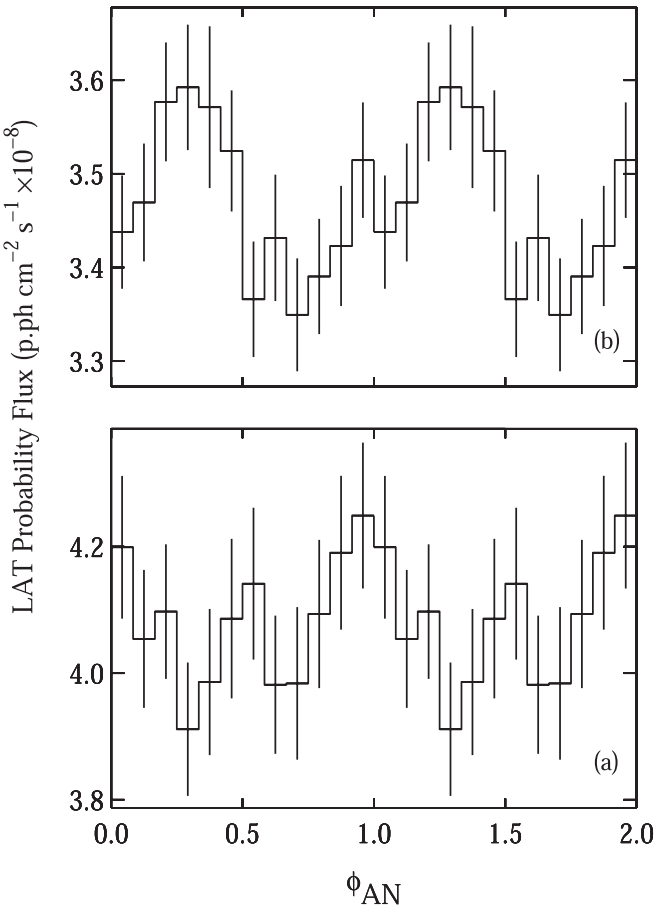

Figure 15. Probability-weighted aperture-photometry LAT light curves of the transitional MSP XSS J12270-4859 (4FGL J1228.0−4853) folded on the orbital period for the time ranges of (a) MJD 54,682-56,250 and (b) MJD 56,250-59,445. Phase zero was defined as 56700.9070772, corresponding to Solution 1 from An (2022).

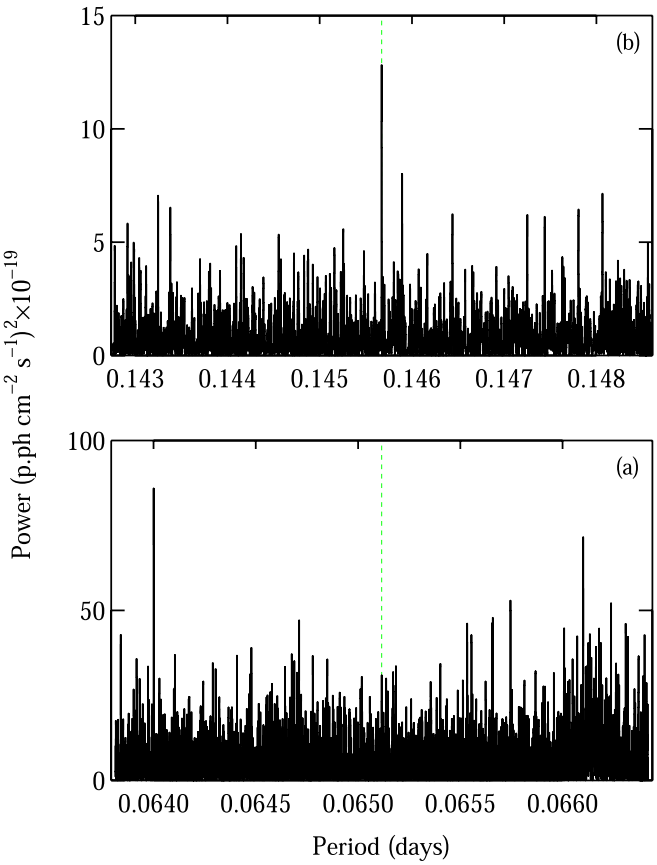

Figure 16. Power spectra of the probability-weighted aperture-photometry LAT light curves of the black widow systems 4FGL J1311.7−3430 (bottom) and 4FGL J2241.7−5236 (top). The orbital periods (Table 5) are marked by the dashed green lines.

start to egress end) is 0.110 ± 0.038 in phase, corresponding to a half-angle of $19\overset{\circ}{.}8 \pm 6\overset{\circ}{.}8$. For comparison, the X-ray eclipse in 4FGL J0427.8−6704 has a half-angle of $12\overset{\circ}{.}5 \pm 0\overset{\circ}{.}3$ (Strader et al. 2016). Chanan et al. (1976) derived eclipse durations for point sources with Roche-lobe filling companions, although these are degenerate between inclination angle and mass ratio, q (mass of the Roche-lobe filling star/mass of the point source). For an inclination angle of 90°, $q \gtrsim 0.25$. Similarly, applying the transit equation of Seager & Mallén-Ornelas (2003) implies a companion mass $>0.85\ M_{\odot}$ to avoid it overfilling its Roche lobe. If, similar to Strader et al. (2016), we consider the possibility that the system could have an inclination as low as 75°, the eclipse duration then requires $q \gtrsim 1$, although this would imply a surprisingly massive companion star. Strader et al. (2019) find a mean mass for redback companions of $0.36 \pm 0.04\ M_{\odot}$ with a σ of $0.15 \pm 0.04\ M_{\odot}$, while black widow companions have companions $<0.05\ M_{\odot}$. If the gamma-ray source is extended, then the constraints on the companion mass are less stringent, but the sharpness of the ingress and egress (∼0.02 in phase) limits the extension of the gamma-ray source to less than $\sim 0.2\ R_{\odot}$, which sets a lower limit on the companion mass of $0.2\ M_{\odot}$. The companion is very unlikely to be less massive, as this would imply a gamma-ray emission size larger than the size of the star, producing a nonzero residual flux during the eclipse and a slower ingress and egress. We conclude that the companion for 4FGL J1702.7−5655 is more likely to be similar to those of redback systems than the very low-mass companions of black widow systems and that, particularly for Part 1, the gamma-ray emission is not highly extended.

For the spider systems with orbital modulation of gamma-ray flux (excluding eclipses by the secondary), there is no definite explanation for this so far. In addition, there is a difference in systems where the modulation is primarily in the pulsed or nonpulsed emission. For 4FGL J2039.5-5617, Ng et al. (2018) suggested that the orbital modulation may be due to Compton scattering of soft photons from the companion and the relativistic pulsar wind. For 4FGL J2339.6−0533, where the pulsed emission is modulated, An et al. (2020) discuss several scenarios, also including Compton scattering from the companion. In 4FGL J1311.7−3430, for the *off*- -pulse orbital modulation at energies >200 MeV, An et al. (2017) discuss bulk plasma motion in the IBS. For systems where quasi-sinusoidal orbital modulation of gamma-ray emission has been reported, this is generally seen to peak near superior conjunction (Table 5), unlike what is expected to be the case for 4FGL J1702.7−5655. 4FGL J1311.7−3430 does show a peak near inferior conjunction. It also exhibits a secondary peak near superior conjunction. Such a secondary peak would be more difficult to detect in 4FGL J1702.7−5655 due to the eclipse.

If 4FGL J1702.7−5655 has not changed between pulsar and accretion regimes, this indicates that some other change has occurred. For the Part 1 light curve, in which the only orbital modulation is the relatively sharp eclipse, we speculate that we

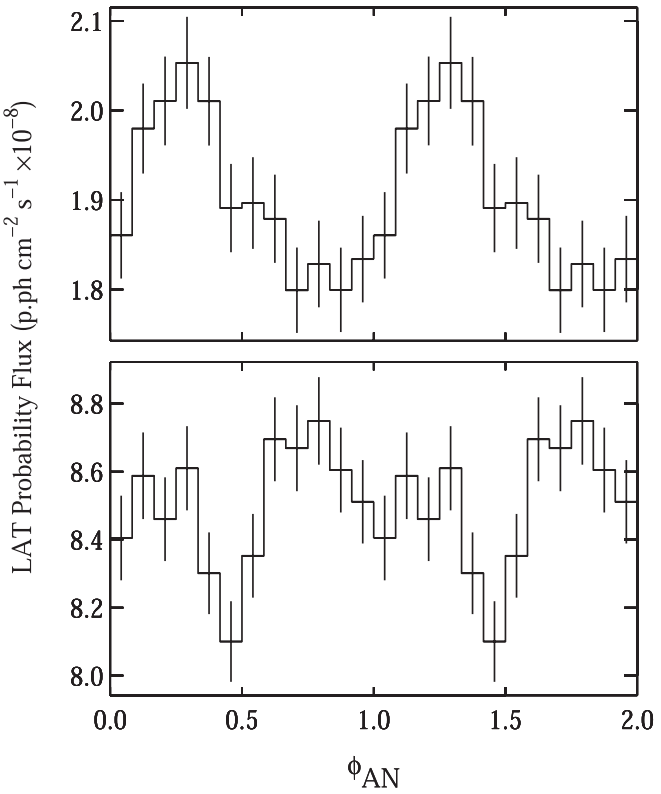

Figure 17. The probability-weighted aperture-photometry LAT light curves of the black widow systems 4FGL J1311.7−3430 (bottom) and 4FGL J2241.7 −5236 (top) folded on their orbital periods (Table 5).

are seeing magnetospheric emission from a pulsar in the system that is not strongly affected by other components in the system. Then, during the second portion of the light curve (i.e., Part 2), some other change occurred in the system. Modulation of the gamma-rays by Compton scattering off the companion star would produce a peak at superior conjunction. However, modulation due to Doppler boosting of the emission produced in the IBS would produce a maximum at inferior conjunction if the pulsar wind is collimated away from the star, wrapping around the pulsar, as is generally observed in redback systems (e.g., An et al. 2020). The change in the modulated light curve would then be due to variability in the IBS emission region. The formation and structure of an IBS in a binary MSP depends on the pressure balances due to winds from the binary components and the pulsar magnetosphere, but the roles of these are still incompletely understood (see e.g., Wadiasingh et al. 2017, 2018; van der Merwe et al. 2020). At least qualitatively, a change in the relative contributions to the gamma-ray emission from a pulsar and an IBS could explain the observed behavior, including the shift in the timing of the eclipse and its duration because the IBS emission is not necessarily centered on the pulsar and has a large spatial extent. However, it is challenging to determine why a change to the IBS occurred, why this should be approximately stable on timescales of years, and why the flux is not substantially changed due to this transition.

There is, however, some observational evidence that changes to the IBS in binary MSPs may occur. Polzin et al. (2020) reported that in low-frequency radio observations of eclipses in the redback system PSR J1816+4510, they found that the radio eclipse mechanism transitioned between one where pulsar emission was removed from the line of sight to one where the pulsations were smeared out. These authors attributed this to a tail of material trailing the pulsar's companion. In the redback 47 Tuc W, Hebbar et al. (2021) found that Chandra observations showed that orbital modulation of X-rays was not always present. They suggested that this was due to changes in the system IBS. For XSS J12270-4859 (4FGL J1228.0-4853), de Martino et al. (2020) found that the orbital X-ray light-curve orbital modulation amplitude varied on timescales of a few months, which might be due to a nonstationary contribution of the IBS. In addition, optical observations of the redback PSR J1048+2339 (4FGL J1048.6 +2340) suggest changes to the IBS on timescales as short as two weeks (Yap et al. 2019). We speculate that the changes in the orbital gamma-ray modulation of 4FGL J1702.7−5655 might be due to similar changes to an IBS to those that occurred in these systems. In 4FGL J1702.7−5655, we have the advantage of the eclipses, which may serve as a way of more precisely determining emission sites. If there is a change in the IBS in 4FGL J1702.7−5655, then measurements of the X-ray orbital variability, and particularly any changes in this associated with a gamma-ray state change, may be a crucial diagnostic.

5. Conclusion

The gamma-ray modulation found in 4FGL J1702.7−5655 is exceptional with its combination of both an eclipse and a quasi-sinusoidal component. The sinusoidal component also has a maximum near inferior conjunction, which is unusual. The change in the orbital profile also appears to be unprecedented, which indicates some change in state, although it is not accompanied by a large change in the gamma-ray flux or spectrum. To better understand the nature of this source, it is important to determine the optical counterpart and its properties, and to conduct long-term multiwavelength monitoring to characterize the changes that occur during the state change and how this may connect to traditional tMSPs. Searches for millisecond pulsations in 4FGL J1702.7−5655 are important, and the determination of Doppler orbits from both pulse timing and optical radial velocity studies are necessary to determine the system parameters, and thus understand the nature of this system. Together with the eclipses, which measure the location of the emission region in the system, these may provide the keys to unlock the physics at work in this system. Continued monitoring of other sources in the Fermi-LAT catalogs has the potential to detect a similar system if the same type of change in its orbital modulation occurs, or the accumulation of additional data might enable the detection of existing modulation. 4FGL J2039.5−5617 should also continue to be monitored to determine whether its quasi-sinusoidal modulation does indeed also change on similar timescales to that in 4FGL J1702.7−5655.

We thank Matthew Kerr and Zorawar Wadiasingh for useful comments. This work was partially supported by NASA Fermi grant 80NSSC21K2029 and also under NASA award number 80GSFC21M0002. J. Strader acknowledges support from a Packard Fellowship. This work was partially supported by NASA grant 80NSSC17K0507 and NSF grant AST-1714825. Portions of this work was performed while S.J.S. held an NRC Research Associateship award at the Naval Research Laboratory. Work at the Naval Research Laboratory is supported by NASA DPR

S-15633-Y. The Australia Telescope Compact Array is part of the Australia Telescope National Facility which is funded by the Australian Government for operation as a National Facility managed by CSIRO, who acknowledge the Gomeroi people as the traditional owners of the Observatory site. We thank the Swift team for undertaking observations and this work made use of data supplied by the UK Swift Science Data Centre at the University of Leicester. The Fermi LAT Collaboration acknowledges generous ongoing support from a number of agencies and institutes that have supported both the development and the operation of the LAT as well as scientific data analysis. These include the National Aeronautics and Space Administration and the Department of Energy in the United States, the Commissariat à l'Energie Atomique and the Centre National de la Recherche Scientifique/Institut National de Physique Nucléaire et de Physique des Particules in France, the Agenzia Spaziale Italiana and the Istituto Nazionale di Fisica Nucleare in Italy, the Ministry of Education, Culture, Sports, Science and Technology (MEXT), High Energy Accelerator Research Organization (KEK) and Japan Aerospace Exploration Agency (JAXA) in Japan, and the K. A. Wallenberg Foundation, the Swedish Research Council and the Swedish National Space Board in Sweden. Additional support for science analysis during the operations phase is gratefully acknowledged from the Istituto Nazionale di Astrofisica in Italy and the Centre National d'Études Spatiales in France.

ORCID iDs

R. H. D. Corbet https://orcid.org/0000-0002-3396-651X
L. Chomiuk https://orcid.org/0000-0002-8400-3705
J. B. Coley https://orcid.org/0000-0001-7532-8359
G. Dubus https://orcid.org/0000-0002-5130-2514
P. G. Edwards https://orcid.org/0000-0002-8186-4753
N. Islam https://orcid.org/0000-0002-2413-9301
J. Strader https://orcid.org/0000-0002-1468-9668
S. J. Swihart https://orcid.org/0000-0003-1699-8867

References

Abdo, A. A., Ackermann, M., Ajello, M., et al. 2010, ApJS, 188, 405
Abdo, A. A., Ajello, M., Allafort, A., et al. 2013, ApJS, 208, 17
Abdollahi, S., Acero, F., Ackermann, M., et al. 2020, ApJS, 247, 33
Acero, F., Ackermann, M., Ajello, M., et al. 2015, ApJS, 218, 23
Ajello, M., Atwood, W. B., Axelsson, M., et al. 2021, ApJS, 256, 12
An, H., Romani, R. W., Johnson, T., et al. 2017, ApJ, 850, 100
An, H., Romani, R. W., & Kerr, M. 2018, ApJL, 868, L8
An, H., Romani, R. W., Kerr, M., et al. 2020, ApJ, 897, 52
An, H. 2022, ApJ, 924, 91
Arzoumanian, Z., Fruchter, A. S., & Taylor, J. H. 1994, ApJL, 426, L85
Atwood, W. B., Abdo, A. A., Ackermann, M., et al. 2009, ApJ, 697, 1071
Bassa, C. G., Patruno, A., Hessels, J. W. T., et al. 2014, MNRAS, 441, 1825
Breton, R. P., van Kerkwijk, M. H., Roberts, M. S. E., et al. 2013, ApJ, 769, 108
Bruel, P., Burnett, T. H., Digel, S. W., et al. 2018, arXiv:1810.11394
Bulgarelli, A., Fioretti, V., Parmiggiani, N., et al. 2019, A&A, 627, A13
Burrows, D. N., Hill, J. E., Nousek, J. A., et al. 2005, SSRv, 120, 165
Camilo, F., Kerr, M., Ray, P. S., et al. 2015, ApJ, 810, 85
Chanan, G. A., Middleditch, J., & Nelson, J. E. 1976, ApJ, 208, 512
Clark, C. J., Wu, J., Pletsch, H. J., et al. 2017, ApJ, 834, 106
Clark, C. J., Nieder, L., Voisin, G., et al. 2021a, MNRAS, 502, 915
Clark, C. J., et al. 2021b, in Ninth Int. Fermi Symp. (Geneva: CERN Indico)
Corbel, S., Dubus, G., Tomsick, J. A., et al. 2012, MNRAS, 421, 2947
Corbet, R. H. D., Chomiuk, L., Coe, M. J., et al. 2016, ApJ, 829, 105
Corbet, R. H. D., Chomiuk, L., Coe, M. J., et al. 2019, ApJ, 884, 93
de Martino, D., Papitto, A., Burgay, M., et al. 2020, MNRAS, 492, 5607
Deneva, J. S., Ray, P. S., Camilo, F., et al. 2016, ApJ, 823, 105
Evans, P. A., Beardmore, A. P., Page, K. L., et al. 2009, MNRAS, 397, 1177
Fermi LAT Collaboration, Ackermann, M., Ajello, M., et al. 2012, Sci, 335, 189
Gentile, P. A., Roberts, M. S. E., McLaughlin, M. A., et al. 2014, ApJ, 783, 69
Goad, M. R., Tyler, L. G., Beardmore, A. P., et al. 2007, A&A, 476, 1401
Grießmeier, J.-M., Smith, D. A., Theureau, G., et al. 2021, A&A, 654, A43
HI4PI Collaboration, Ben Bekhti, N., Flöer, L., et al. 2016, A&A, 594, A116
Hebbar, P. R., Heinke, C. O., Kandel, D., et al. 2021, MNRAS, 500, 1139
Horne, J. H., & Baliunas, S. L. 1986, ApJ, 302, 757
Kandel, D., Romani, R. W., & An, H. 2019, ApJ, 879, 73
Kennedy, M. R., Breton, R. P., Clark, C. J., et al. 2020, MNRAS, 494, 3912
Kerr, M. 2011, ApJ, 732, 38
Kerr, M. 2019, ApJ, 885, 92
Kong, A. K. H., Takata, J., Hui, C. Y., et al. 2018, MNRAS, 478, 3987
Lampton, M., Margon, B., & Bowyer, S. 1976, ApJ, 208, 177
Levine, A. M., Bradt, H. V., Chakrabarty, D., et al. 2011, ApJS, 196, 6
Miller, J. M., Swihart, S. J., Strader, J., et al. 2020, ApJ, 904, 49
Ng, C. W., Takata, J., Strader, J., et al. 2018, ApJ, 867, 90
Nolan, P. L., Abdo, A. A., Ackermann, M., et al. 2012, ApJS, 199, 31
Papitto, A., & de Martino, D. 2022, in Millisecond Pulsars, ed. S. Bhattacharyya et al. (Berlin: Springer International)
Polzin, E. J., Breton, R. P., Bhattacharyya, B., et al. 2020, MNRAS, 494, 2948
Roberts, M. S. E. 2013, Proc. IAU, 291, 127
Roberts, M. S. E., Mclaughlin, M. A., Gentile, P., et al. 2014, AN, 335, 313
Romani, R. W., & Shaw, M. S. 2011, ApJL, 743, L26
Roy, J., Ray, P. S., Bhattacharyya, B., et al. 2015, ApJL, 800, L12
Seager, S., & Mallén-Ornelas, G. 2003, ApJ, 585, 1038
Sault, R. J., Teuben, P. J., & Wright, M. C. H. 1995, in Astronomical Data Analysis Software and Systems IV, ASP Conf. Ser. 77 (San Fransisco, CA: ASP), 433
Saz Parkinson, P. M., Xu, H., Yu, P. L. H., et al. 2016, ApJ, 820, 8
Scargle, J. D. 1982, ApJ, 263, 835
Stovall, K., Lynch, R. S., Ransom, S. M., et al. 2014, ApJ, 791, 67
Strader, J., Li, K.-L., Chomiuk, L., et al. 2016, ApJ, 831, 89
Strader, J., Swihart, S., Chomiuk, L., et al. 2019, ApJ, 872, 42
Stroh, M. C., & Falcone, A. D. 2013, ApJS, 207, 28
van der Klis, M. 1989, in Timing Neutron Stars: Proc. of the NATO Advanced Study Institute on Timing Neutron Stars, ed. H. Ögelman & E. P. J. van den Heuvel (New York: Kluwer Academic/Plenum Publishers), 27
van der Merwe, C. J. T., Wadiasingh, Z., Venter, C., et al. 2020, ApJ, 904, 91
VanderPlas, J. T. 2018, ApJS, 236, 16
Vaughan, S. 2005, A&A, 431, 391
Wadiasingh, Z., Harding, A. K., Venter, C., et al. 2017, ApJ, 839, 80
Wadiasingh, Z., Venter, C., Harding, A. K., et al. 2018, ApJ, 869, 120
Wilson, W. E., Ferris, R. H., Axtens, P., et al. 2011, MNRAS, 416, 832
Wu, E. M. H., Takata, J., Cheng, K. S., et al. 2012, ApJ, 761, 181
Wu, J., Clark, C. J., Pletsch, H. J., et al. 2018, ApJ, 854, 99
Xing, Y., & Wang, Z. 2015, ApJL, 804, L33
Xing, Y., & Wang, Z. 2015, ApJ, 808, 17
Yap, Y. X., Li, K. L., Kong, A. K. H., et al. 2019, A&A, 621, L9
Yaqoob, T. 1998, ApJ, 500, 893
Zechmeister, M., & Kürster, M. 2009, A&A, 496, 577